The Astrophysical Journal Letters, 982:L38 (15pp), 2025 April 1 https://doi.org/10.3847/2041-8213/adbd46

MIRI-LRS Spectrum of a Cold Exoplanet around a White Dwarf: Water, Ammonia, and Methane Measurements

Maël Voyer[1], Quentin Changeat[2,3], Pierre-Olivier Lagage[4], Pascal Tremblin[5], Rens Waters[6,7,8], Manuel Güdel[9,10], Thomas Henning[11], Olivier Absil[12], David Barrado[13], Anthony Boccaletti[14], Jeroen Bouwman[11], Alain Coulais[4,15], Leen Decin[16], Adrian M. Glauser[10], John Pye[17], Alistair Glasse[18], René Gastaud[19], Sarah Kendrew[20], Polychronis Patapis[10], Daniel Rouan[14], Ewine F. van Dishoeck[21], Göran Östlin[22], Tom P. Ray[23], and Gillian Wright[24]

[1] Université Paris Cité, Université Paris-Saclay, CEA, CNRS, AIM, F-91191 Gif-sur-Yvette, France; mael.voyer@u-paris.fr
[2] Kapteyn Institute, University of Groningen, 9747 AD Groningen, The Netherlands
[3] Department of Physics and Astronomy, University College London, Gower Street, WC1E 6BT, UK
[4] Université Paris-Saclay, Université Paris Cité, CEA, CNRS, AIM, F-91191 Gif-sur-Yvette, France
[5] Université Paris-Saclay, UVSQ, CNRS, CEA, Maison de la Simulation, 91191, Gif-sur-Yvette, France
[6] SRON Netherlands Institute for Space Research, Niels Bohrweg 4, 2333 CA Leiden, The Netherlands
[7] Department of Astrophysics/IMAPP, Radboud University, PO Box 9010, 6500 GL Nijmegen, The Netherlands
[8] HFML—FELIX. Radboud University, PO Box 9010, 6500 GL Nijmegen, The Netherlands
[9] Department of Astrophysics, University of Vienna, Türkenschanzstrasse 17, 1180 Vienna, Austria
[10] ETH Zürich, Institute for Particle Physics and Astrophysics, Wolfgang-Pauli-Strasse 27, 8093 Zürich, Switzerland
[11] Max-Planck-Institut für Astronomie (MPIA), Königstuhl 17, 69117 Heidelberg, Germany
[12] STAR Institute, Université de Liège, Allée du Six Août 19c, 4000 Liège, Belgium
[13] Centro de Astrobiología (CAB), CSIC-INTA, ESAC Campus, Camino Bajo del Castillo s/n, 28692 Villanueva de la Cañada, Madrid, Spain
[14] LESIA, Observatoire de Paris, Université PSL, CNRS, Sorbonne Université, Univ. Paris Diderot, Sorbonne Paris Cité, 5 place Jules Janssen, 92195 Meudon, France
[15] LERMA, Observatoire de Paris, Université PSL, Sorbonne Université, CNRS, Paris, France
[16] Institute of Astronomy, KU Leuven, Celestijnenlaan 200D, 3001 Leuven, Belgium
[17] School of Physics & Astronomy, Space Park Leicester, University of Leicester, 92 Corporation Road, Leicester, LE4 5SP, UK
[18] UK Astronomy Technology Centre, Royal Observatory, Blackford Hill, Edinburgh EH9 3HJ, UK
[19] Université Paris-Saclay, CEA, Département d'Electronique des Détecteurs et d'Informatique pour la Physique, 91191, Gif-sur-Yvette, France
[20] European Space Agency, Space Telescope Science Institute, Baltimore, MD 21218, USA
[21] Leiden Observatory, Leiden University, P.O. Box 9513, 2300 RA Leiden, The Netherlands
[22] Department of Astronomy, Oskar Klein Centre, Stockholm University, 106 91 Stockholm, Sweden
[23] Astronomy & Astrophysics Section, School of Cosmic Physics, Dublin Institute for Advanced Studies, 31 Fitzwilliam Place, Dublin, D02 XF86, Ireland
[24] UK Astronomy Technology Centre, Royal Observatory Edinburgh, Blackford Hill, Edinburgh EH9 3HJ, UK
Received 2024 December 21; revised 2025 February 17; accepted 2025 March 4; published 2025 March 25

Abstract

The study of the atmosphere of exoplanets orbiting white dwarfs is a largely unexplored field. With WD 0806-661 b, we present the first deep dive into the atmospheric physics and chemistry of a cold exoplanet around a white dwarf. We observed WD 0806-661 b using JWST's Mid-InfraRed Instrument Low-Resolution Spectrometer, covering the wavelength range from 5 to 12 μm, and the Imager, providing us with 12.8, 15, 18, and 21 μm photometric measurements. We carried the data reduction of those data sets, tackling second-order effects to ensure a reliable retrieval analysis. Using the TauREx retrieval code, we inferred the pressure–temperature structure, atmospheric chemistry, mass, and radius of the planet. The spectrum of WD 0806-661 b is shaped by molecular absorption of water, ammonia, and methane, consistent with a cold Jupiter atmosphere, allowing us to retrieve their abundances. From the mixing ratio of water, ammonia, and methane we derive $C/O = 0.34 \pm 0.06$, $C/N = 14.4^{+2.5}_{-1.8}$, and $N/O = 0.023 \pm 0.004$ and the ratio of detected metals as a proxy for metallicity. We also derive upper limits for the abundance of CO and CO_2 (1.2×10^{-6} and 1.6×10^{-7}, respectively), which were not detected by our retrieval models. While our interpretation of WD 0806-661 b's atmosphere is mostly consistent with our theoretical understanding, some results—such as the lack of evidence for water clouds, an apparent increase in the mixing ratio of ammonia at low pressure, or the retrieved mass at odds with the supposed age—remain surprising and require follow-up observational and theoretical studies to be confirmed.

Unified Astronomy Thesaurus concepts: Direct imaging (387); Spectroscopy (1558); Exoplanet atmospheres (487); James Webb Space Telescope (2291); Bayesian statistics (1900)

Materials only available in the online version of record: machine-readable table

1. Introduction

Due to its unprecedented sensitivity and unique wavelength coverage, JWST has opened a new window into the characterization of Y dwarfs ($T_{\rm eff} < 500$ K) and low-temperature exoplanets (D. Barrado et al. 2023; S. A. Beiler et al. 2023;

J. Rigby et al. 2023; H. Kothari et al. 2024; H. Kühnle et al. 2024). Previously, such objects were mainly observed using ground-based instruments, and mid-infrared spectroscopy was unavailable. Recently, studies of VHS-1256-1257b by JWST demonstrated the pivotal capabilities of the telescope in the infrared and its accurate absolute flux calibration (B. E. Miles et al. 2020, 2023). JWST enables spectroscopic observations of much colder and fainter planetary-mass self-luminous objects—with similar characteristics to solar system objects—which is of particular interest to the exoplanet community.

One such intriguing object is WD 0806-661 b (hereafter WD 0806 b), a planetary-mass companion orbiting a white dwarf (WD) at an apparent separation of 2500 au (K. L. Luhman et al. 2011, 2012). Planetary systems around WDs have been the subject of many studies (D. Veras 2021; U. Malamud 2024). Polluted WDs, debris disks, and dust disks allow us to study the composition of destroyed exoplanets and planetesimals (B. T. Gänsicke et al. 2012; S. Xu et al. 2019; L. K. Rogers et al. 2024). Yet atmospheres of planets around WDs remain difficult to characterize, with so far only a single directly observed exoatmosphere in a WD system (WD 1856+534 b). This particular object did not show molecular features (R. Alonso et al. 2021; S. Xu et al. 2021). Accordingly, WD 0806 b is a unique opportunity to study the atmospheres of exoplanets around WDs.

Based on evolutionary models (A. Burrows et al. 2003; D. Saumon & M. S. Marley 2008) using the system age of 2 ± 0.5 Gyr (J. P. Subasavage et al. 2009), the comparison of observed magnitudes in J band (m_J) and in a Spitzer band ($m_{[4.5]}$) suggests that WD 0806 b has an effective temperature of $T_{\rm eff} \sim 300$–345 K and a mass of $M_p \in [6, 9] M_J$ (K. L. Luhman et al. 2012). In this Letter, we present a newly acquired spectrum of WD 0806 b, obtained by JWST's MIRI Low-Resolution Spectrometer (LRS) and the F1280W, F1500W, F1800W, and F2100W filters of MIRI's Imager (P. Bouchet et al. 2015; G. H. Rieke et al. 2015; G. S. Wright et al. 2023). The data were acquired as part of the GTO 01276 (PI: Lagage) on 2023 July 14. WD 0806 b is the first planetary-mass object around a WD to unveil molecular features through direct spectroscopy.

Our analysis of WD 0806 b starts from the raw data. Our data reduction pipeline, which relies on the official STScI steps along with customized functions, and our retrieval setup are described in Section 2. Our retrieval results are shown in Section 3. Finally, Section 4 provides additional discussion on the implications and robustness of our findings.

2. Methodology

2.1. Observations

The observations of WD 0806 b were taken by the Mid-InfraRed Instrument Low-Resolution Spectrometer (MIRI-LRS; $R \approx 100$) using a two-dither pattern, the source being too faint for MIRI Mid-Resolution Spectrometer (MIRI-MRS). Each slit position was exposed for 1.79 hr (one exposure with eight integrations of 290 groups in FASTR1 mode). The availability of two slit positions is in principle advantageous for background and detector systematics subtraction. The standard practice is to subtract the detector images from the two exposures, leaving a positive and negative spectral trace. Using the MIRI Imager, we also observed WD 0806 b with the 12.8, 15, 18, and 21 μm filters for 277, 560, 283, and 283 s, respectively (i.e., 50, 50, 25, and 25 groups in 1, 2, 2, and 2 integrations using the FASTR1 mode).

2.2. Data Reduction of the MIRI-LRS Data

For Stages 1 and 2 of the data reduction, we mostly utilize the official JWST STScI pipeline. We used the most recent version at the time of the reduction: pipeline 1.12.5 and the Calibration Reference Data System (CRDS) 11.17.14. However, we modified the steps pertaining to error propagation, outlier rejection, background subtraction, and wavelength calibration to optimally process our data, and we did not use Stage 3 at all.

Stage 1. The first stage (i.e., detector level correction) is set up using the default parameters of the STScI pipeline, except for the reset step, which is merged with the dark current subtraction step. We then use the Stage 1 output "rateints" files to perform a customized background subtraction. Details are described in Appendix A.1.

Stage 2. After the custom background subtraction, we apply the default Stage 2 step from the STScI JWST pipeline, providing us with the "calints" files. We perform our outlier detection and interpolation at the end of Stage 2. Details are in Appendix A.2.

New step, "background rescaling." We add a new step at the end of Stage 2 to rescale inconsistent flux levels (i.e., offsets) between the two slit positions. Figure 1 shows the flux offsets originating from the background before the application of this step. Integrations within the same exposures are consistent, which suggests that the discrepancy arises from a varying background between the two slit positions. Discussions with instrument experts at STScI have led to the hypothesis that light coming from the MIRI Imager—which is close to saturation at the end of each integration—could spread to the LRS subarray differently owing to the slight change in field of view (i.e., $\sim 1\farcs5$).[25]

In preparation for further statistical analysis (i.e., atmospheric retrievals), this issue needs to be corrected: for direct imaging, absolute flux and nonastrophysical wavelength-dependent signals can strongly bias parameter estimates. To remove the background, we make use of the two dither positions (i.e., as done by the default STScI step). As shown in Figure 1, too much background appears to be subtracted for the first dither, and too little for the second dither. We perform a rescaling correction by applying a wavelength-dependent factor inferred by fitting a second-order polynomial to the median background pixels (see Appendix A.3).

Stage 3. We apply a customized Stage 3 step to extract and combine the spectra from the different images. Our extraction aperture is a rectangular, 6 pixels wide, box centered on the spectral trace. The step is performed *individually* for each integration, and several corrections are applied (the details are available in Appendix A.4).

2.3. Data Reduction of the MIRI Filters Data

Additionally, four observations of WD 0806 b were obtained with the MIRI filters F1280, F1500, F1800, and F2100. We use the STScI pipeline to reduce these data sets and get the "cal" files. The source at 21 μm could not be detected by the STScI pipeline. We did detect it using a custom flux extraction, background subtraction,

[25] Our data set is dominated by a background with a right-to-left gradient (see Figure 5). However, zodiacal light—the dominant source of sky background for $\lambda \in [5, 12]$ μm (W. T. Reach et al. 2003; J. Pyo et al. 2010)—is expected to be spatially constant in the 2.4 arcsec^2 field of view of the LRS slit (J. Pyo et al. 2012), and therefore it cannot explain the changing background.

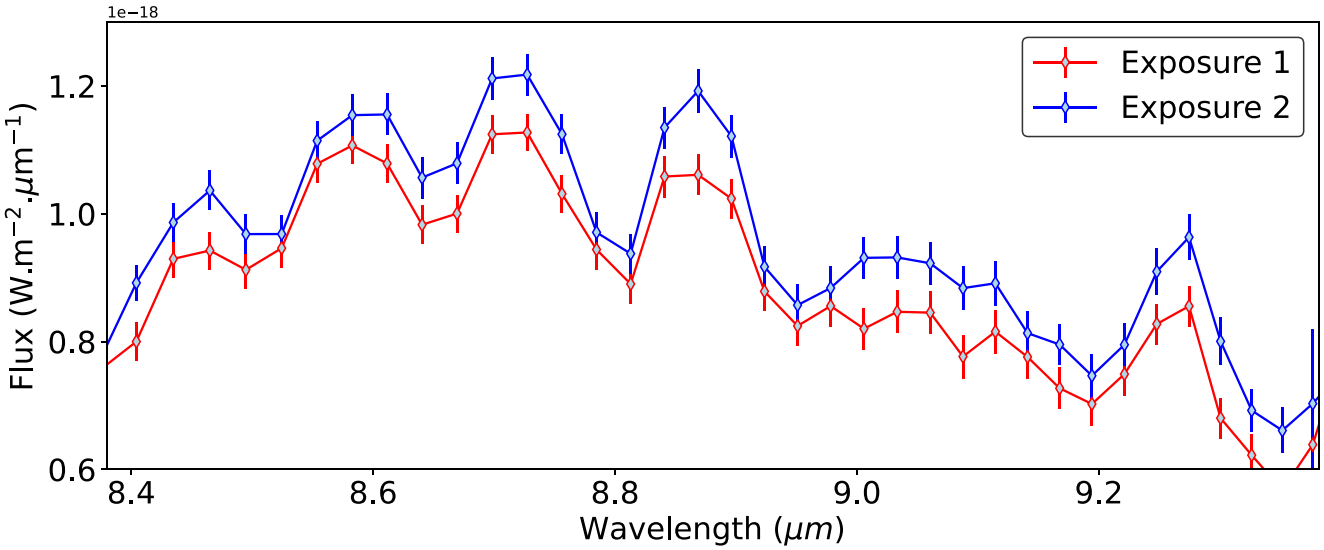

Figure 1. Extracted spectra from exposure 1 (red) and exposure 2 (blue). We show a zoom-in of the spectra for better visibility.

and aperture correction. Using Photutils, we used a circular aperture to sum the flux coming from the source and an annulus aperture to measure the background level. The radii of these apertures were taken from the JWST CRDS file *jwst_miri_apcorr_*0010 for proper aperture correction. For consistency, this custom step is applied to all four filters. In the cases where the STScI pipeline can detect the target, our extracted fluxes using the custom step are within the uncertainties of the values from the STScI pipeline. For F1280, F1500, F1800, and F2100 we obtain the photometric fluxes F_p={5.8±0.1,4.75±0.08,3.0±0.1,2.1±0.3}×10^{-19} W m^{-2} μm^{-1}, respectively.

2.4. Atmospheric Retrieval

Once the spectrum is obtained, we extract the information content using the TauREx3 atmospheric retrieval code (A. F. Al-Refaie et al. 2021, 2022).

The retrievals are performed on the *LRS data only* since incompatibilities between data sets—from planet variability (B. E. Miles et al. 2023; Q. Changeat et al. 2024) and instrument systematics (K. H. Yip et al. 2021; B. Edwards et al. 2024)—are known to be possible. At native pixel resolution, spectral lines are spread by the optics onto several pixels in the spectral direction. Analyzing the data at native resolution, we need to account for that effect. We utilize the TauREx-multimodel[26] plug-in (Q. Changeat et al. 2025), which allows convolving the high-resolution theoretical spectrum with the line-spread function of the instrument.

The planet is modeled with a plane-parallel atmosphere of 80 layers spanning the pressures $p \in [10^6, 0.1]$ Pa in log space, assuming hydrostatic equilibrium. We use a hydrogen/helium atmosphere with a solar ratio of 0.17. For radiatively active species, we use the cross sections at resolution $R = 50{,}000$ from the ExoMol project (J. Tennyson et al. 2016; K. L. Chubb et al. 2021). We included absorption from water (O. L. Polyansky et al. 2018), ammonia (S. N. Yurchenko et al. 2011), methane (S. N. Yurchenko & J. Tennyson 2014), carbon monoxide (G. Li et al. 2015), carbon dioxide (S. N. Yurchenko et al. 2020), and phosphine (C. Sousa-Silva et al. 2015). Each abundance is freely retrieved with molecular mixing ratio either constant with altitude or with a two-layer profile (see Q. Changeat et al. 2019). We include collision-induced absorption (CIA) from H_2–H_2 (M. Abel et al. 2011; L. N. Fletcher et al. 2018) and H_2–He (M. Abel et al. 2012) and Rayleigh scattering (A. N. Cox 2015). Aerosols are considered using the TauREx-PyMieScatt[27] plug-in (Q. Changeat et al. 2025). TauREx-PyMieScatt allows the inclusion of parameterized aerosols using their wavelength-dependent optical constants. Given the predicted and retrieved thermal structure (see Figure 3), we considered water-ice clouds and ammonia-ice clouds (D. Curtis et al. 2005; C. J. A. Howett et al. 2007)—similar in composition to Jupiter's clouds—and fully opaque gray clouds. In this study, condensate species such as salt clouds and silicate clouds, commonly often discussed in brown dwarf studies, were excluded since our temperature regimes are much colder. For the parameter exploration, we used uniform priors as described in Appendix C and sampled the parameter space using the nested sampling algorithm MultiNest (F. Feroz et al. 2009; J. Buchner et al. 2014). MultiNest is set up with an evidence tolerance of 0.5 and 2000 live points. We here define the core retrievals for our analysis:

1. *Baseline setup*. H_2O, NH_3, and CH_4 constant through the atmosphere.
2. *Best setup*. H_2O and CH_4 constant through the atmosphere. Two-layer NH_3.
3. *Five-species setup*. H_2O, CH_4, CO, and CO_2 constant through the atmosphere. Two-layer NH_3. No other molecule.
4. *Cloudy setup*. H_2O and CH_4 constant through the atmosphere. Two-layer NH_3. H_{2O} ice and NH_3 ice clouds.
5. *Free water setup*. Constant CH_4. Two-layer NH_3 and H_2O.[28]

[26] The code and documentation can be found at https://github.com/groningen-exoatmospheres/taurex-multimodel.

[27] The code and documentation can be found at https://github.com/groningen-exoatmospheres/taurex-pymiescatt.

[28] The atmosphere is too hot for methane condensation, so we did not explore a two-layer profile for that specie.

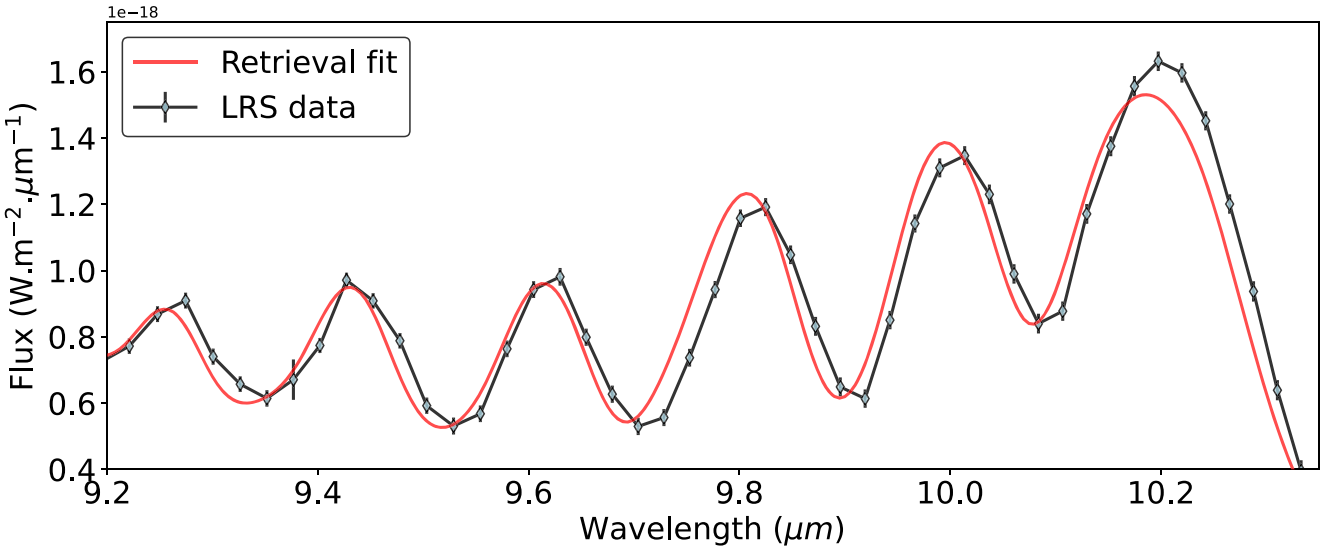

Figure 2. LRS spectrum using the default wavelength calibration (black) and best fit from TauRex (red). A wavelength discrepancy ($\Delta\lambda \sim 10$ nm) is clearly visible.

2.5. Wavelength Calibration

In our first set of retrievals, results showed a definite, wavelength-dependent mismatch between line positions of the data and the theoretical models (see Figure 2, bottom panel). This phase shift is below the current wavelength calibration level of MIRI-LRS (i.e., $\Delta\lambda \sim 20$ nm) and therefore consistent with expected instrument design specifications. Contributions to this mismatch between data and theoretical spectra could also come from uncertainties in the cross sections, albeit unlikely to be of major importance. In any case, the spectra need a wavelength correction to ensure that the inferred atmospheric parameters are not biased by this effect. We therefore fitted for the wavelength solution using a third-order[29] polynomial correction. The best-fit correction for our data is given by

$$\lambda_{\rm shifted} = -1.15 \cdot 10^{-5} \cdot \lambda^3 + \lambda, \quad (1)$$

where $\lambda_{\rm shifted}$ is the corrected wavelength solution and λ the unmodified one, both in microns. We provide a table with the adopted wavelength solution in Appendix B, Table 1.

We then fixed that correction for all retrievals for consistency. This correction results in much higher Bayesian evidence (hereafter E) with $\Delta\ln(E) \approx 300$ compared to the same fits without correction, and it impacts the retrieved parameters. Given the Bayesian evidence difference, we emphasize the need for precise calibration and systematic checks when performing atmospheric retrieval exercises with JWST data.

3. Results

The spectrum shape of WD 0806 b is as expected and consistent with other observed Y0 dwarfs (J. A. Zalesky et al. 2019; D. Barrado et al. 2023; S. A. Beiler et al. 2023, 2024; H. Kühnle et al. 2024). We have clear detection of three molecules, NH_3, H_2O, and CH_4 with $\Delta\ln(E) = 5504$, $\Delta\ln(E) = 3540$, and $\Delta\ln(E) = 15{,}364$, respectively (see Figure 6 and R. E. Kass & A. E. Raftery 1995).

[29] We tested polynomials with orders from one to five and found that third order is the lowest order that could best explain the data.

Figure 3 shows the results from the "best setup" described in Section 2.5, which we utilize in this section. Note that this retrieval uses the MIRI-LRS data from $\lambda \in [5, 11.7]$ μm only. The photometric data ($\lambda \in \{12.8, 15, 18, 21\}$ μm) are also plotted in the inset of Figure 3 to showcase the predictive power of the fit at longer wavelengths. The photometric data match the forward model at 0.12σ, 1.4σ, 0.95σ, and 0.20σ, respectively, providing us with additional confidence in our retrieval results.

In this section, we present the consistent results (within 3σ) across all setups outlined in Section 2.5.

The pressure region $p = [1, 0.01]$ bars constitutes ~81.6% of our information content (see Figure 4). This region is therefore well constrained. Our retrievals yield a decreasing-with-altitude temperature profile, from $T = 547^{+39}_{-49}$ K at $p = 1$ bar to $T = 118^{+67}_{-57}$ K at $p = 10^{-2}$ bars. The probability density distributions for water, methane, and ammonia in Figure 4 exhibit mixing ratio values of $\log(H_2O) = -3.19^{+0.08}_{-0.07}$, $\log(CH_4) = -3.58^{+0.07}_{-0.06}$, and $\log(NH_3) = -4.74^{+0.08}_{-0.07}$, respectively, with their $\pm3\sigma$ limits. These abundances all fall into the range observed for other Y0 dwarfs (J. A. Zalesky et al. 2019; D. Barrado et al. 2023; H. Kothari et al. 2024).

The contribution function shows that 18.1% of the data informs us about the atmosphere at $p < 0.01$ bars. The information at such pressures comes from the NH_3, H_2O, and CH_4 lines between $\lambda \in [5.7, 8.0]$ μm and the two ammonia lines between $\lambda \in [10, 11]$ μm. For $p \in [0.01, 10^{-4}]$ bars, the $T - p$ profile is consistent with isothermal at 1σ (see the black region in Figure 4).

At high altitude ($p < 10^{-4}$ bars) and up to the top of our domain ($p = 10^{-6}$ bars) the $T - p$ shows a negative lapse rate (i.e., thermal inversion). Specifically, the retrieved median model shows a ~200 K increase from $T = 154^{+89}_{-87}$ K at $p = 10^{-4}$ bars to $T = 381^{+37}_{-43}$ K at $p = 10^{-5}$ bars. This increase produces additional flux for the lines mentioned above. However, we note that this thermal inversion is weak, and the 3σ temperature profile remains consistent with isothermal. Such thermal inversions could be present, even in a low irradiation regime such as WD 0806 b, due to, e.g., breaking of gravity waves, or diabatic convection (S. K. Leggett et al. 2019; P. Tremblin et al. 2019; S. K. Leggett & P. Tremblin 2023).

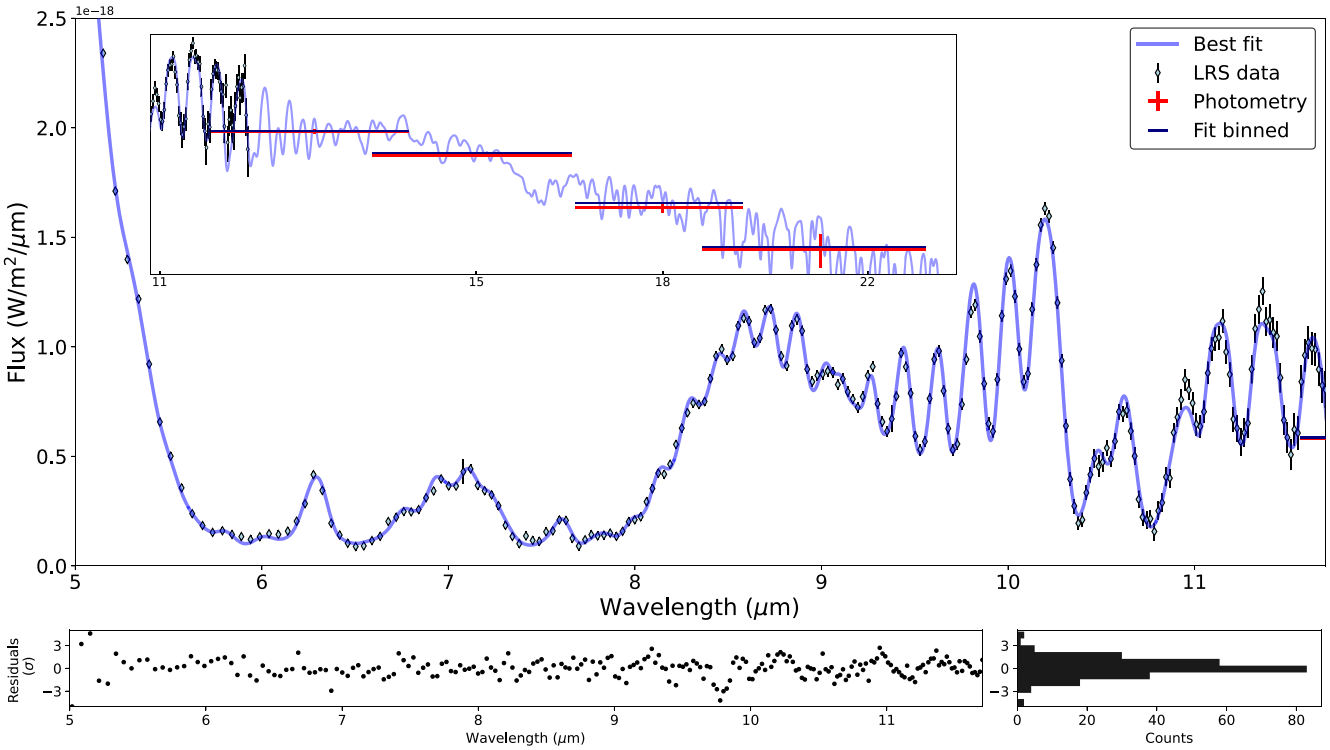

Figure 3. Top panel: MIRI fixed-slit LRS spectrum of WD 661 b (black) and best-fit model from TauREx (blue). The black rectangle in the upper left corner shows the $\lambda = [11, 24]$ μm range. The red lines are the $\lambda \in \{12.8, 15, 18, 21\}$ μm photometric points from MIRI. They are not included in the retrieval, just plotted over the best fit. The navy line at the same places corresponds to the best fit, binned to the resolution of these photometric points. The bottom left panel displays the residuals between the LRS data and the best fit, for which the root mean standard deviation is 1.247. The bottom right panel shows the histograms of these residuals.

When using a two-layer profile for ammonia (see, e.g., best setup, cloudy setup, five-species setup, and free setup), the high-altitude layer is systematically retrieved with a mixing ratio[30] of $\log(\mathrm{NH_3\ top}) = -2.5^{+1.5}_{-0.9}$ (see the dashed green line in Figure 4). The mass retrieved is $M_p = 0.51^{+0.57}_{-0.2} M_\mathrm{J}$ (3σ uncertainties). For the radius, our best setup retrieves $R_p = 1.12^{+0.07}_{-0.07} R_\mathrm{J}$, which is stable across the different setups mentioned above. We note that the planetary mass is outside the expected mass range from formation and evolutionary models. The ammonia gradient is also physically unexpected given the $T - p$ range. These points are discussed more in Sections 4.2 and 4.4. Despite the retrieved $T - p$ profile crossing the condensation curve of water (see Figure 4), our retrieval does not find evidence for clouds, providing us with an upper limit of $\log(P_\mathrm{clouds}) > 3.2^{+6.8}_{-2.4}$ bars.

Except H_2O, NH_3, and CH_4, we do not find evidence for other major opacity sources. We do not detect CO and CO_2: the five-species setup infers upper limits of $\log(\mathrm{CO}) < -5.9$ and $\log(\mathrm{CO_2}) < -5.3$. These molecules do not have significant absorption lines in the range of MIRI-LRS, making their detection challenging. However, CO_2 has a strong feature at 15 μm, so the photometric data can be used to obtain a stricter constraint. We search for such a stricter constraint by increasing the mixing ratio of CO_2 in our best-fit model until its absorption leads to 5σ departure in the F1500W filter. That method provides a mixing ratio upper limit of $\log(\mathrm{CO_2}) < -6.8$.

In the 4 hr spanning our LRS observations, we do not detect significant planetary variability: all our integrations are compatible with each other (see Figure 9). Additionally, we note that the photometric data were taken about 1 day before the MIRI-LRS data, and they appear consistent with our best-fit forward model. Hence, the emission from the planet's atmosphere appears stable over the 24 hr period of our observations.

4. Discussion

4.1. Clouds

Extending our best-fit model to $\lambda \in [0.3, 51.4]$ μm,[31] we compute the effective temperature of WD 0806 b to be $T_\mathrm{eff} = 343 \pm 11$ K. Hence, we explored the possibility of condensation for the species we detect, i.e., H_2O, NH_3, and CH_4. Using the condensation curve from K. Lodders & B. Fegley (2002) and our retrieved pressure−temperature profile, we determine that only water is likely to condense, while ammonia's condensation is less probable (see Figure 4). The condensation curve from K. Lodders & B. Fegley (2002) depends on the atmosphere's metallicity. As we do not have access to that parameter, we use a range $Z \in [0.1, 10]\ Z_\odot$ to estimate the pressure range where water should condense. We derived that water should condense at a pressure between $p \in [3.5 \times 10^{-2}, 6.2 \times 10^{-2}]$ depending on the metallicity. However, 60% of our information comes from below 6×10^{-2} bars. Hence, if water condenses and forms significant clouds, we should detect it.

We searched for water and ammonia ice cloud signatures by adding their absorption properties using the Mie scattering code

[30] Proportion of the molecule in the gas.

[31] The molecule's cross-sectional wavelength ranges.

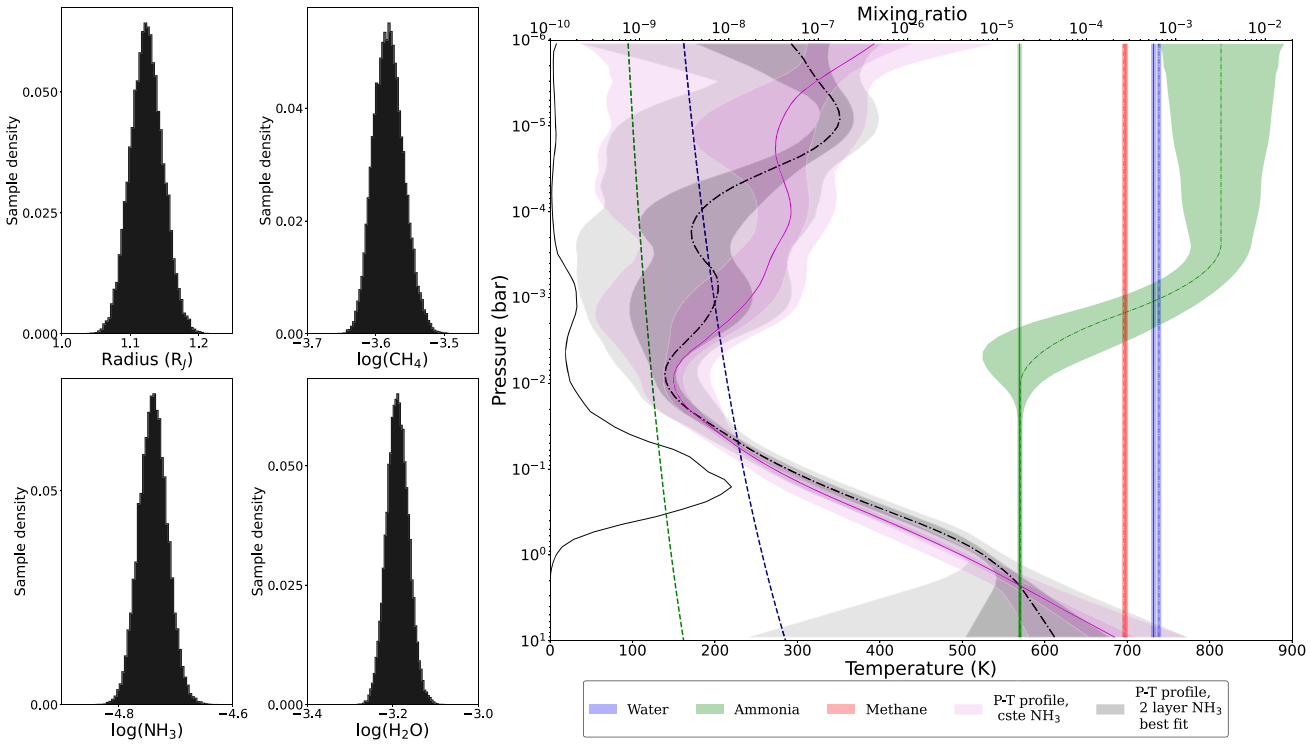

Figure 4. Summary of the main retrieval results from our best setup. Left panel: histograms of the final samples for the radius and mixing ratios of CH_4, H_2O, and NH_3 from the best setup. Right panel: pressure–temperature profile from the best setup (black) and for the baseline retrieval with constant NH_3 (purple); both corner plots are in Appendix D, Figures 7 and 8. The chemical profiles, with a 1σ region, of water (blue), ammonia (green), and methane (red) are shown with a dashed line for the best setup and with solid lines for the baseline setup. The navy and green dashed lines show water and ammonia condensation curves for solar metallicity from K. Lodders & B. Fegley (2002). The black solid line is the radiative contribution function for the best setup.

PyMieScatt (B. J. Sumlin et al. 2018). This is included in TauREx via the TauREx-PyMieScatt plug-in (Section 2.4). This corresponding cloudy setup reached $\ln(E) = 10386$, a positive difference of 1 compared to our best setup, which is not significant (R. E. Kass & A. E. Raftery 1995). We therefore prefer the simpler cloudless model with eight fewer free parameters (R. Trotta 2008). To further push our investigations, and considering that clouds might not extend in a sufficiently wide pressure range to produce major spectral features on our emission spectrum (D. Curtis et al. 2005; C. J. A. Howett et al. 2007), we also study a rainfall mechanism that sequesters water from the gas phase. This is implemented by using a two-layer profile for water (free water setup). The retrieved mixing ratio profile for water in this case is unconstrained at $p < 0.01$ bars. The retrieved profile is consistent with a constant with altitude mixing ratio and $\Delta\ln(E) = -1.3$; hence, we prefer the simpler model with a constant water profile (R. Trotta 2008). Note that we attempted to force a high-altitude water depletion by fixing $\log(H_2O_{top}) = -12$ and obtained $\Delta\ln(E) = -1.7$. Again, a constant mixing ratio for water is preferred.

Our retrievals do not provide significant evidence for the presence of clouds in the atmosphere of WD 0806 b. Our observation and retrievals could be compatible with a rainfall mechanism involving a thin cloud layer. However, as with the clouds, a simpler constant with altitude abundance is statistically favored. While MIRI-MRS could probe a lower pressure range, this source is too faint (D. Barrado et al. 2023; H. Kühnle et al. 2024). NIRSpec could access the $\lambda = 3.5$ μm water ice feature and help us understand the formation of clouds in exoplanets.

4.2. Robustness of the NH_3 Gradient and Relation to the Mass Estimates

Below 0.01 bars, all retrievals systematically converge toward a mixing ratio consistent with $\log(NH_3^{surf}) = -4.74^{+0.08}_{-0.07}$[32] as shown in Figure 7. However, we achieve the highest Bayesian evidence for retrievals with a positive ammonia gradient through the atmosphere. This gradient is statistically significant, as the difference in Bayesian evidence between the best setup and the baseline setup is $\Delta\ln(E) = 23.5$. The best setup favors a mixing ratio at the top of the atmosphere at $\log(NH_3^{top}) = -2.5^{+1.5}_{-0.9}$. However, we did not find a physically convincing explanation for this increase in the ammonia mixing ratio. The retrieved $T - p$ profile does not allow for the N_2/NH_3 conversion reaction to be significant, and the flux from the WD is estimated to be too weak ($\approx 10^{-9}$ W) to significantly induce photochemical reactions.

Besides the ammonia chemistry, the major change arising from having a two-layer ammonia profile is a stricter constraint of the planet's mass. For example, the best setup yields $M_P = 0.51^{+0.57}_{-0.2} M_J$, whereas the baseline setup gives $M_P = 0.75^{+1.0}_{-0.30} M_J$ ($\pm 3\sigma$). This can easily be explained because the mass changes the pressure scale of the planet. The pressure of the ammonia gradient adds a constraint on the pressure scale compared to a constant mixing ratio of ammonia. Hence, as the pressure scale is better constrained, the mass constraint is stricter. Using retrievals, we show that higher masses result in the gradient located at higher pressures, whereas lower masses result in a NH_3 gradient higher in the atmosphere. At the 3σ

[32] This is the value from the best setup with 3σ errors.

level, the gradient's mid-pressure is constrained between $\log(p_{NH_3}) = 2.2^{+0.7}_{-3.1}$ Pa.

As this ammonia gradient is statistically significant, we report it, but given the lack of physical explanation, this point should be taken with caution. Given the correlation between the mass constraint and the ammonia gradient, we prefer to use the wider mass estimates from the baseline setup.

4.3. Element Ratios

WD 0806 b orbits a WD on a wide-separation (i.e., semimajor axis $a \geqslant 1300$ au), unknown orbit. We derive the atmospheric elemental ratios to compare WD 0806 b with other known Y0 dwarfs. As the host star is a WD, we do not have access to the progenitor main-sequence star's element ratios (J. P. Subasavage et al. 2009). Hence, we cannot easily use the following ratio to conclude on the probable formation path of the planet. Nevertheless, from the water, ammonia, and methane abundances reported in Figure 4 we derive estimates for C/O, C/N, and N/O. Using K. Lodders & B. Fegley (2002) and given our retrieved $T - p$ profile, we establish that NH_3, H_2O, and CH_4 are the major gas-bearing species for N, O, and C, respectively. S. Fonte et al. (2023) showed that oxygen entrapment in refractory species changes with equilibrium temperature and metallicity. However, as our temperature range is not covered, we settle on a middle value of 20% entrapment in refractory species between the estimate of K. Lodders & B. Fegley (2002) and that of S. Fonte et al. (2023). For the nitrogen content, we do not consider the increase in ammonia at high altitude, given the low pressure the amount of additional nitrogen is negligible. We derive $C/O = 0.34 \pm 0.06$, $C/N = 14.4^{+2.5}_{-1.8}$, and $N/O = 0.023 \pm 0.004$. The derived C/O ratio is similar to those observed in known Y0 dwarfs (J. A. Zalesky et al. 2019; D. Barrado et al. 2023; H. Kothari et al. 2024; Z. Tu et al. 2024). Moreover, using $Z = (C + N + O)/H$ as a proxy for metallicity, we find a slightly subsolar metallicity. More specifically, $Z = 0.74^{+0.13}_{-0.09} \cdot Z_{\odot}^{CNO}$ with $Z_{\odot}^{CNO} = (C_{\odot} + N_{\odot} + O_{\odot})/H_{\odot}$ (M. Asplund et al. 2009).

4.4. Consistency of the Mass and Radius with Evolutionary Models

We use the models from M. S. Marley et al. (2021) to obtain another estimate of WD 0806 b's mass from evolutionary models. Using the retrieval-independent system's age quoted in K. L. Luhman et al. (2012), 2 ± 0.5 Gyr, and the effective temperature of $T_{\rm eff} = 343 \pm 11$ K computed by integrating the flux of our forward model, we obtain a predicted planetary mass of $M_p \in [6.3, 9.4] M_J$. This is inconsistent with our retrieved mass of $M_p \in [0.45, 1.75] M_J$ (see Table 2). Note that our estimated effective temperature is one of the most robust parameters we derive and matches the findings from K. L. Luhman et al. (2012) obtained via Spitzer photometry. We identify three possible sources for the above discrepancies in radius, mass, and effective temperature.

(1) *Our retrieved mass is incorrect.* Assumptions made in the retrievals—such as the opacity source treatment, 1D plane-parallel atmosphere, or free chemistry—could bias the retrieved value of the mass.
(2) *The age used for evolutionary model predictions is incorrect.* If the retrieved mass is correct, it matches the evolutionary track of a much younger object (60–180 Myr old). Such a young age would require that WB 0806 b formed after its host star, as could be the case for a captured object.
(3) *Assumptions of the evolutionary models do not apply to this case.* The evolutionary models could be neglecting important opacity sources, affecting cooling rates (A. Burrows et al. 2007). Other possibilities could include unaccounted-for energy sources, or the planet being a binary (J. W. Xuan et al. 2024). We are able to exclude tidal heating as a likely additional heating source, as the periapsis is at least 10 au.[33] Additionally, the stellar flux is too weak ($\approx 10^{-9}$ W) for the stellar irradiation to be a sufficient source of heat.

The retrieved radius ($R_p = 1.12^{+0.07}_{-0.07} R_J$; see Table 2) is consistent with a planet with an age of 2 ± 0.5 Gyr and a mass of $M_p \in [6.3, 9.4] M_J$ (i.e., the retrieved mass would be incorrect), but also with a much younger (60–180 Myr) and lighter planet with $M_p \in [0.45, 1.75] M_J$ (i.e., the age estimate would be incorrect).

A stricter constraint on the radius, 1% instead of the current 6.5%, could help distinguish the young object scenario from the old one. The joint retrieval analysis of both MIRI and NIRSpec could help provide such a stricter constraint.

5. Conclusion

We reduced the MIRI-LRS data of WD 0806-661 b, modifying the background subtraction step, adding a new background rescaling step, and using a custom-made extraction. The TAUREX fit of the extracted spectrum yields precise constraints on the water, methane, and ammonia mixing ratio, as well as the $T - p$ profile of this atmosphere. While the $T - p$ profile allows for condensation of water, our search for signatures of aerosols did not favor this scenario: a cloud-free model is preferred. Using the forward model, we compute the precise effective temperatures of the planet and place upper limits on the abundance of carbon monoxide and carbon dioxide. Our retrievals yield a smaller-than-expected planetary mass, which is at odds with evolutionary model tracks based on the WD progenitor's age. However, this smaller mass is consistent with a younger object formed later than the host's system. The radius we derive is consistent with both scenarios; following analysis with additional NIRSpec data will help us select the correct explanation. Further study, potentially using more self-consistent atmospheric models or relying on complementary data with NIRSpec, can allow us to assess the robustness of these parameters and place further constraints on CO and CO_2 abundances.

Acknowledgments

The authors thank the anonymous referee for helpful comments, improving the quality of the paper. The authors thank G. Sloan, B. Trahin, M. Regan, and the other STScI experts for their precious inputs and knowledge of MIRI and the STScI pipeline. M.V. extends his gratitude to L. Pueyo for providing funds for a 2-month collaboration at STScI and S. Schleich and A. Dyrek for insightful discussions on retrieval methods and pipeline development. M.V. is also grateful to E. Matthews for her help in finding the Sonora models. P-O.L.

[33] We used the most favorable orbital parameters with an eccentricity and a of 0.99 and 1300 au, respectively.

and M.V. acknowledge funding support by CNES. This publication is part of the project "Interpreting exoplanet atmospheres with JWST" with file No. 2024.034 of the research program "Rekentijd nationale computersystemen" that is (partly) funded by the Netherlands Organisation for Scientific Research (NWO) under grant doi:10.61686/QXVQT85756. This work used the Dutch national e-infrastructure with the support of the SURF Cooperative using grant No. 2024.034. D.B. is supported by Spanish MCIN/AEI/10.13039/501100011033 grants PID2019-107061GB-C61 and PID2023-150468NB-I00. O.A. is a Senior Research Associate [Research Director] of the Fonds de la Recherche Scientifique—FNRS. O.A. thanks the European Space Agency (ESA) and the Belgian Federal Science Policy Office (BELSPO) for their support in the framework of the PRODEX Programme. J.P. acknowledges financial support from the UK Science and Technology Facilities Council and the UK Space Agency. G.Ö. acknowledges support from the Swedish National Space Agency (SNSA). This work is based on observations made with the NASA/ESA/CSA James Webb Space Telescope. The data were obtained from the Mikulski Archive for Space Telescopes at the Space Telescope Science Institute, which is operated by the Association of Universities for Research in Astronomy, Inc., under NASA contract NAS5-03127 for JWST. These observations are associated with program No. 1276. The specific observations analyzed can be accessed via DOI:10.17909/anme-j453. This project was provided with computing HPC and storage resources by GENCI at TGCC thanks to grant 2024-15722 on the supercomputer Joliot Curie's SKL and ROME partition. For the purpose of open access, the authors have applied a Creative Commons Attribution (CC BY) license to the Author Accepted Manuscript version arising from this submission.

Facility: JWST (MIRI-LRS Fixed Slit and MIRI Imager).

Software: TauREx (A. F. Al-Refaie et al. 2021, 2022), MultiNest (F. Feroz et al. 2009; J. Buchner et al. 2014), PyMultiNest (J. Buchner et al. 2014), JWST Pipeline (H. Bushouse et al. 2024), Photutils (L. Bradley et al. 2024).

Appendix A
Pipeline Modifications

A.1. Background Subtraction

The pipeline—version 1.12.5—we use does not include error propagation from the background subtraction step.[34] We therefore create a custom background subtraction step to include this additional error term. We start by building the background images with the half-images, from the "rateints" files, that do have the target signal (like the right-hand side of the left panel of Figure 5). Scanning pixel by pixel, we perform a 5σ clip on the integrations to reject temporal outliers. If a value is flagged, it is replaced by the mean of the integrations. If an NaN (white pixels in Figure 5, left panel)[35] is present in all integrations, we interpolate it. To that effect, we average the integrations together to fit a second-order[36] polynomial to the line (cross-dispersion direction) and recover the value. The error of these recovered pixels is estimated as the average of the two neighboring pixels' error (in the cross-dispersion direction). We use this time outlier and NaN-free averaged image from one exposure for our background subtraction. This background image from one exposure is subtracted from the integrations of the other exposure, with proper error propagation.

A.2. Outlier Interpolation of the Science Images

After Stage 2, we remove the temporal and spatial outliers from the science images. This step begins by identifying temporal outliers within each exposure (eight integrations per exposure, so we compare eight values). For each value, we calculate the median and standard deviation (std) by excluding one value at a time from the eight-value set, performing this calculation eight times. We then compute the median of these medians and standard deviations, which we refer to as the "master median" and "master std." Using these metrics, we apply a 5σ clip to the full set of eight values, removing any outliers. This method offers improved robustness over a standard 5σ clip, which can be skewed by extreme outliers. The identified outliers are replaced with the mean of the remaining data set.

Our data contain a number of spatial outliers (i.e., outliers present on every integration; isolated dark-red points in Figure 5). They are detected using a 5σ clip with their eight direct neighbors (3×3 corona). Such outliers can create a charge spillage effect, where they affect the values of their direct neighbors. We perform for each of the center pixel direct neighbors a 5σ clip on the 5×5 corona to detect such contamination and replace all flagged pixels with NaNs.

A.3. Background Rescaling

As seen in Figure 1, the flux levels of the source in the different exposures do not match. To correct this, we introduce an additional "Background rescaling" step. Working on the "calints" files after the outlier interpolation exposed above in Appendix A.2, we mask both positive and negative traces (image area impacted by the target's signal), with an 11-pixel-wide rectangle. Given that the images are 42 pixels wide and that we use two 11-pixel-wide masks per image, each remaining line has 20 pixels. To perform a robust statistical treatment, we merge the arrays of the eight integrations together so that the combined lines are $8 \times 20 = 160$ pixels wide. For each line of these 160-pixel-wide images, we compute the line-by-line medians in the cross-dispersion direction (see, e.g., the right panel of Figure 5). Those medians, therefore, capture the wavelength-dependent variation of the background's gradient in the two exposures (i.e., corresponding to the two source positions). A second-order polynomial is then fitted to these medians (right panel of Figure 5) to smooth our background solution. Finally, line by line, the associated polynomial's value is subtracted from the pixels' signal.

A.4. Spectral Extraction

To extract the spectra from the individual integrations, we utilize the "calints" files, after correction by our "outlier interpolation" and our "Background Rescaling" step described in Appendices A.2 and A.3. We utilize a 6-pixel-wide rectangular aperture or a 4-pixel-wide aperture if NaNs are present in the two edge pixels. When NaNs occur within the central 4 pixels, we interpolate them using a Gaussian function (on the cross-dispersion direction). For this Gaussian

[34] https://jwst-pipeline.readthedocs.io/en/latest/jwst/error_propagation/main.html

[35] We keep the warm and hot pixels, as they are present in the other exposure.

[36] Second order needed to fit the shape of the background gradient.

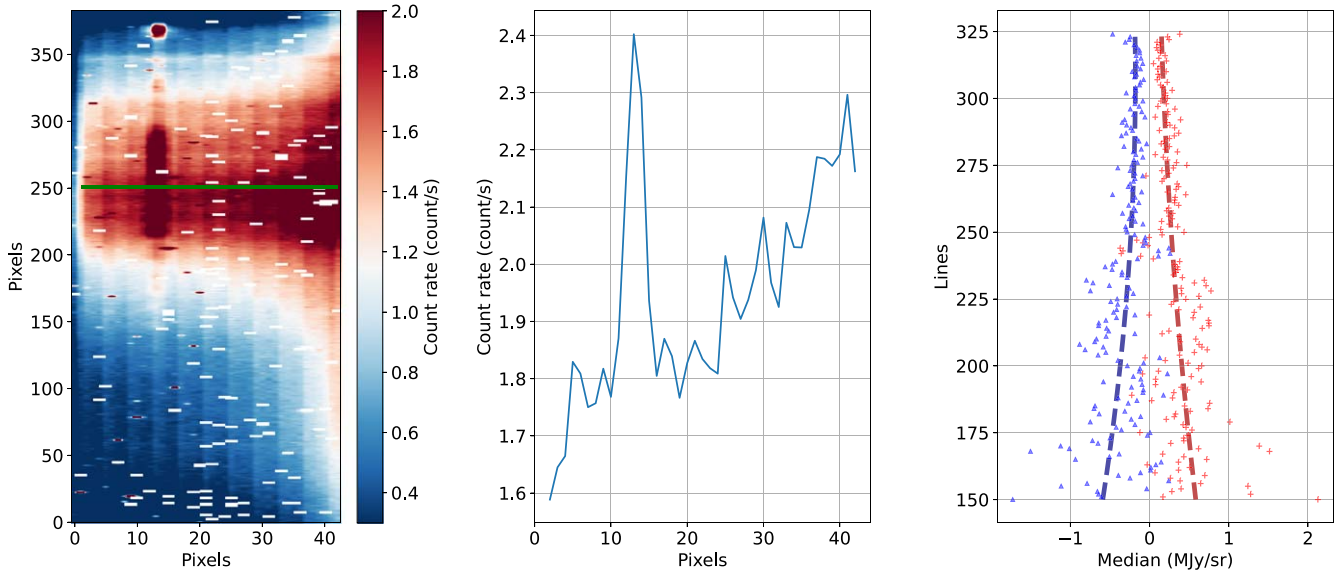

Figure 5. Left panel: mean image of the first exposure after the ramp fitting. Middle panel: plot of the green line shown in the left panel. We clearly see the right-to-left gradient and the target's signal. Right panel: line-by-line median for each of the two exposures and associated second-order polynomial fit.

interpolation—because of the curved trace—we fix the mean of the Gaussian function to the center of the trace, which is obtained by fitting second-order polynomials to the NaN-free lines. If the Gaussian has a standard deviation smaller than the length of the line, we use it to interpolate the missing value. However, if multiple NaNs are present in the center of the trace, we discard the entire line, as there is insufficient information to reliably recover the missing values. In that case, the data point on the final spectrum will come from only one exposure (the spectrum error also reflects this). Lastly, we extract accounting for the finite aperture using the standard "jwst_miri_apcorr_0012" file. The integrations are then combined, followed by the exposures, to produce the final spectra presented in Figure 3.

Appendix B
Wavelength Solution

This appendix contains in Table 1 the adopted wavelength correction for this study.

Table 1
Row Number with the Associated Wavelength Adopted in This Study

Row Number		Wavelength (μm)
MIRIm Coordinates	LRS Coordinates	
393	1	3.12478
392	2	3.62459
391	3	3.79141
…	…	…
8	386	13.95934
7	387	13.97298
6	388	13.98651

Note. Row numbers, labeled Yrow, are given in both MIRIm coordinates (Yrow $\in$ [1, 2024]) and LRS Slit coordinates from calibration file "jwst_miri_specwcs_0008.fits" (Yrow $\in$ [1, 388]). The full table is available in the journal version of this paper.

(This table is available in its entirety in machine-readable form in the online article.)

Appendix C
Retrieval Priors

Here we present Table 2, which contains the priors and retrieved parameters for the best setup and baseline setup retrievals.

Table 2
Priors Used for Our Retrievals and Best Setup and Baseline Setup Posteriors with 3σ Limits

Parameters	Priors	Retrieved Parameters	
		Best Setup	Baseline Setup
R_P	$\mathcal{U} \in [0.5-2]\ R_{\rm P}$	$1.12^{+0.07}_{-0.07}$ $R_{\rm J}$	$1.18^{+0.08}_{-0.08}$ $R_{\rm J}$
M_P	$\mathcal{U} \in [0.3-10]\ M_{\rm P}$	$0.51^{+0.57}_{-0.2}$ $M_{\rm J}$	$0.75^{+1.1}_{-0.3}$ $M_{\rm J}$
$T_{\rm Surf}$	$\mathcal{U} \in [20-1000]$ K	615^{+169}_{-389}K	693^{+94}_{-110}K
T_1	$\mathcal{U} \in [20-1000]$ K	547^{+39}_{-49}K	504^{+30}_{-47}K
T_1	$\mathcal{U} \in [20-1000]$ K	227^{+30}_{-35}K	261^{+24}_{-39}K
T_1	$\mathcal{U} \in [20-1000]$ K	118^{+67}_{-57} K	126^{+75}_{-55} K
T_4	$\mathcal{U} \in [20-1000]$ K	215^{+127}_{-195}K	250^{+101}_{-229}K
T_5	$\mathcal{U} \in [20-1000]$ K	154^{+89}_{-87} K	305^{+101}_{-279} K
T_6	$\mathcal{U} \in [20-1000]$ K	381^{+37}_{-43} K	263^{+170}_{-242} K
$T_{\rm Top}$	$\mathcal{U} \in [20-1000]$ K	289^{+51}_{-122} K	399^{+163}_{-373} K
$NH_{3\ \rm Surface}$	$\mathcal{U} \in [10^{-8}-10^{-1}]$	$-4.74^{+0.08}_{-0.07}$	$-4.74^{+0.08}_{-0.06}$
$NH_{3\ \rm Top}$	$\mathcal{U} \in [10^{-8}-10^{-1}]$	$-2.5^{+1.5}_{-0.9}$	Not in model
$NH_{3\ \rm P}$	$\mathcal{U} \in [10^{6}-0.1]$ Pa	$2.2^{+0.7}_{-3.1}$ Pa	Not in model
CH_4	$\mathcal{U} \in [10^{-8}-10^{-1}]$	$-3.58^{+0.07}_{-0.06}$	$-3.56^{+0.08}_{-0.06}$
H_2O	$\mathcal{U} \in [10^{-8}-10^{-1}]$	$-3.19^{+0.08}_{-0.07}$	$-3.25^{+0.1}_{-0.08}$
Flat Mie	$\mathcal{U} \in [10^{6}-0.1]$ Pa	$>5.5^{+0.5}_{-0.6}$ Pa	$>5.6^{+0.4}_{-0.5}$ Pa

Note. Molecules' volume mixing ratios and pressures in $\log_{10}$ scale.

Appendix D
Additional Figures

This appendix contains the complementary figures to Section 3, Figures 6–9.

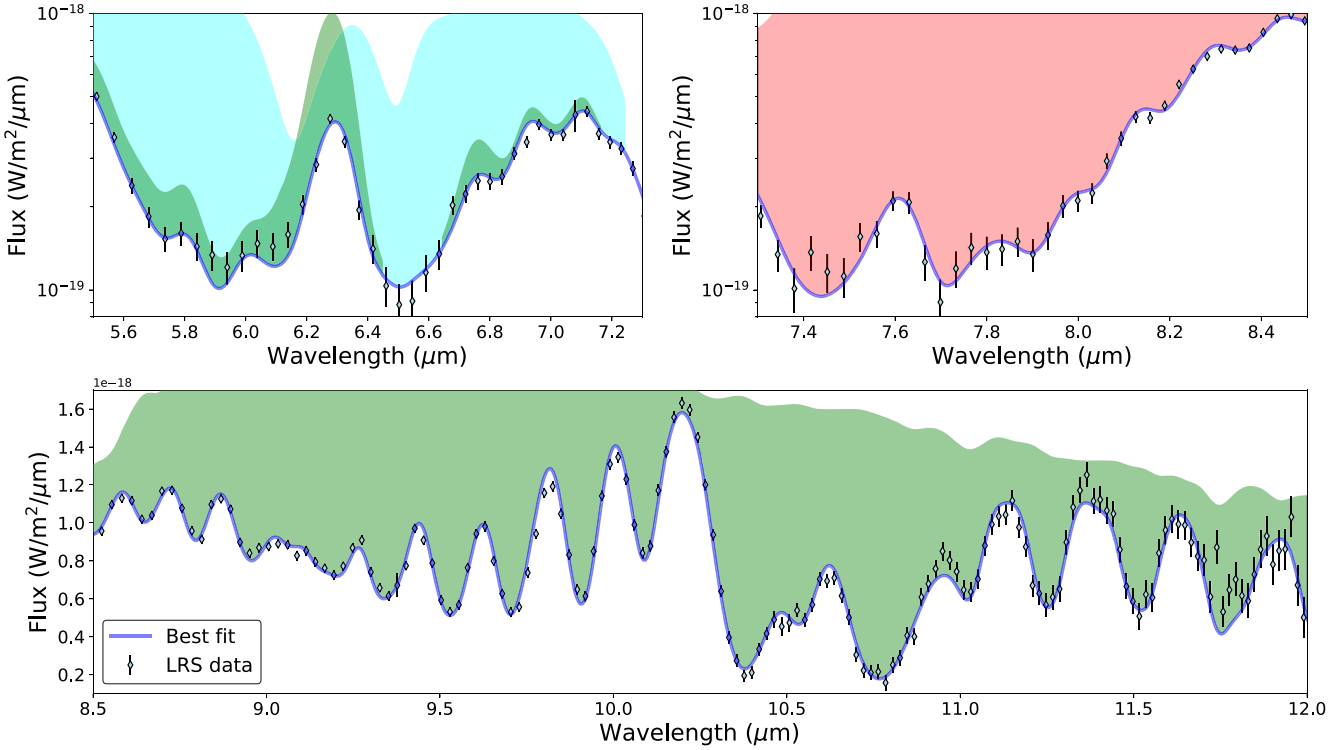

Figure 6. Molecular absorption created by water (blue), ammonia (green), and methane (red).

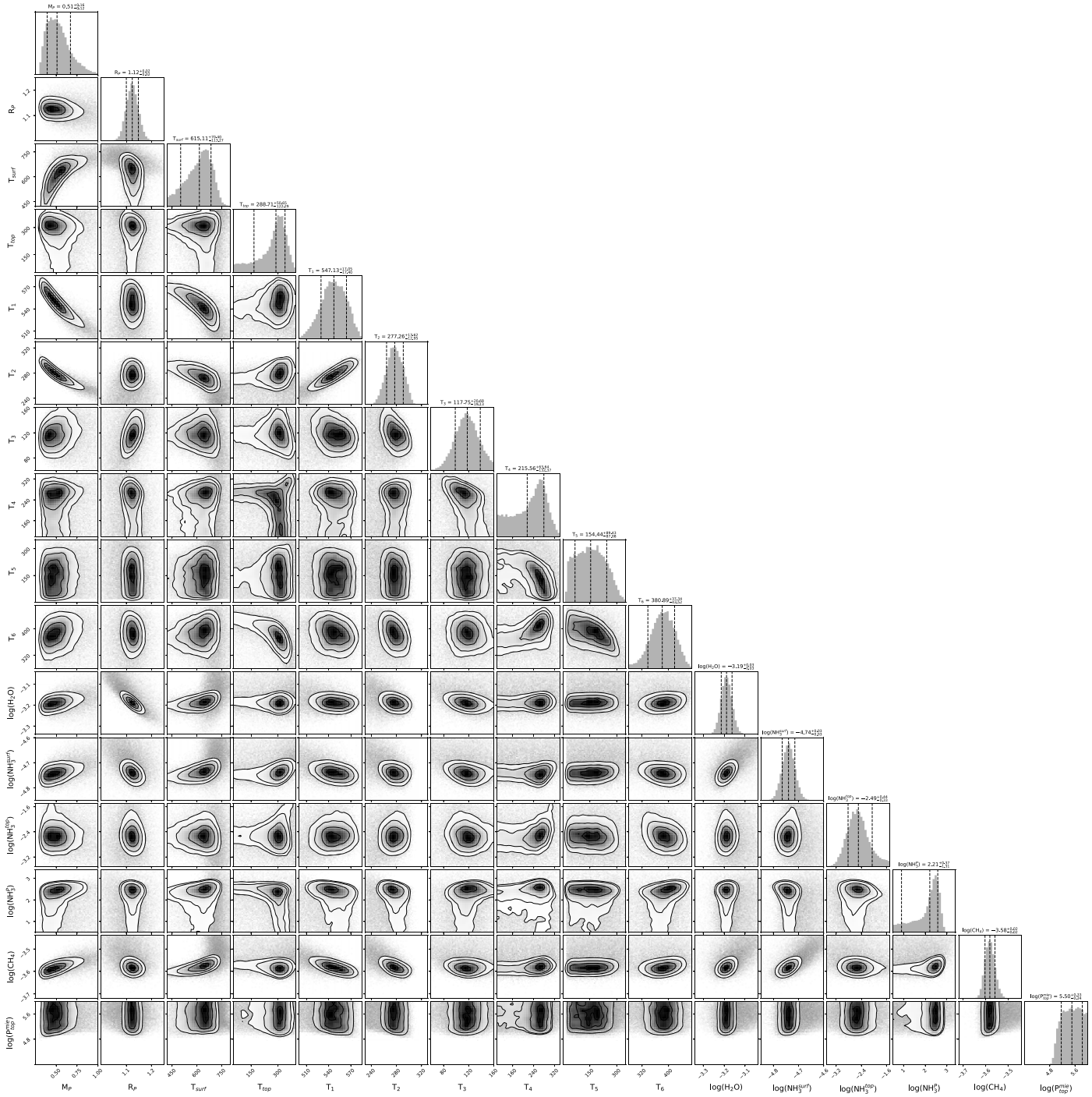

Figure 7. Corner plot for our best setup.

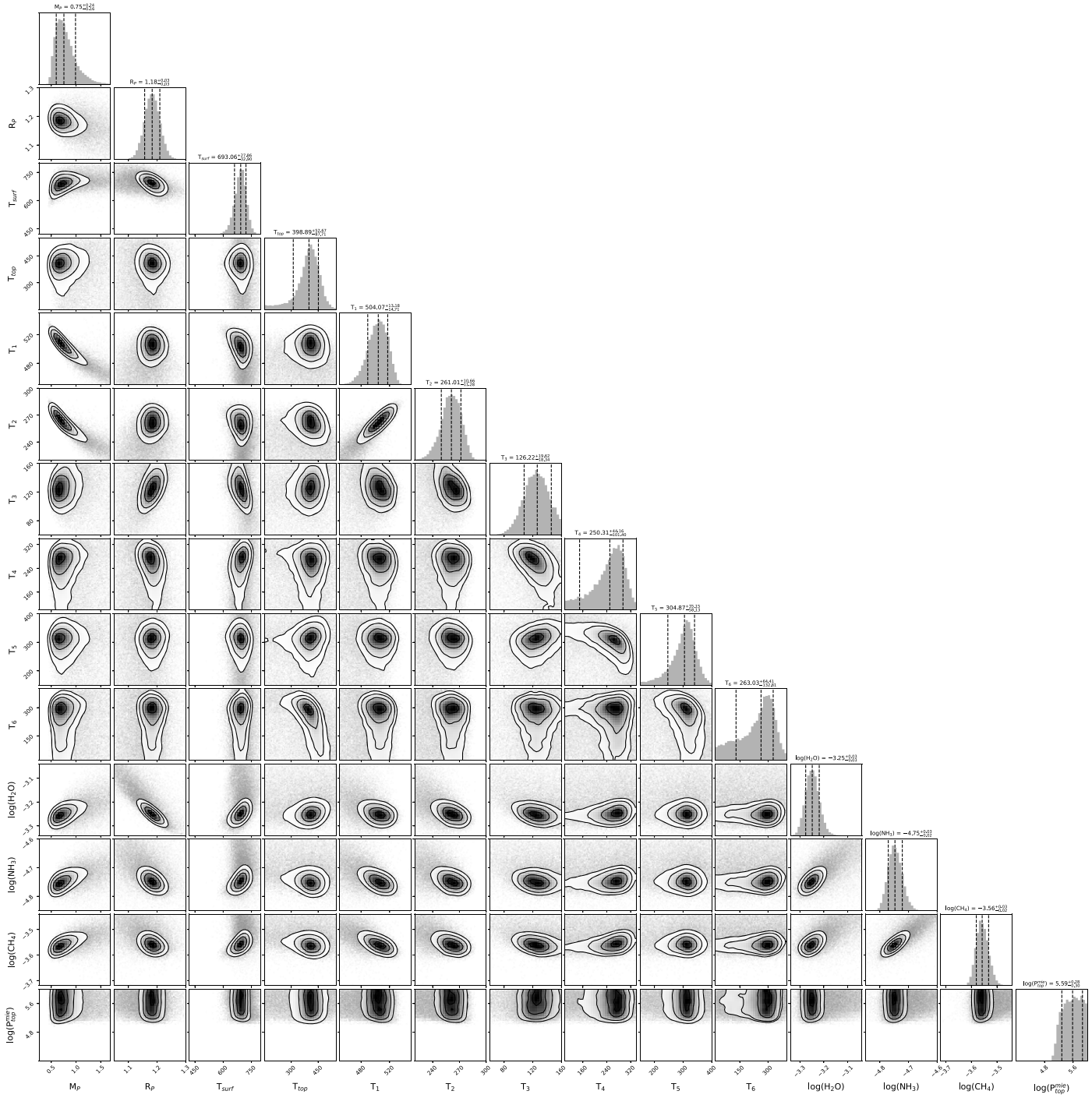

Figure 8. Corner plot for our baseline setup.

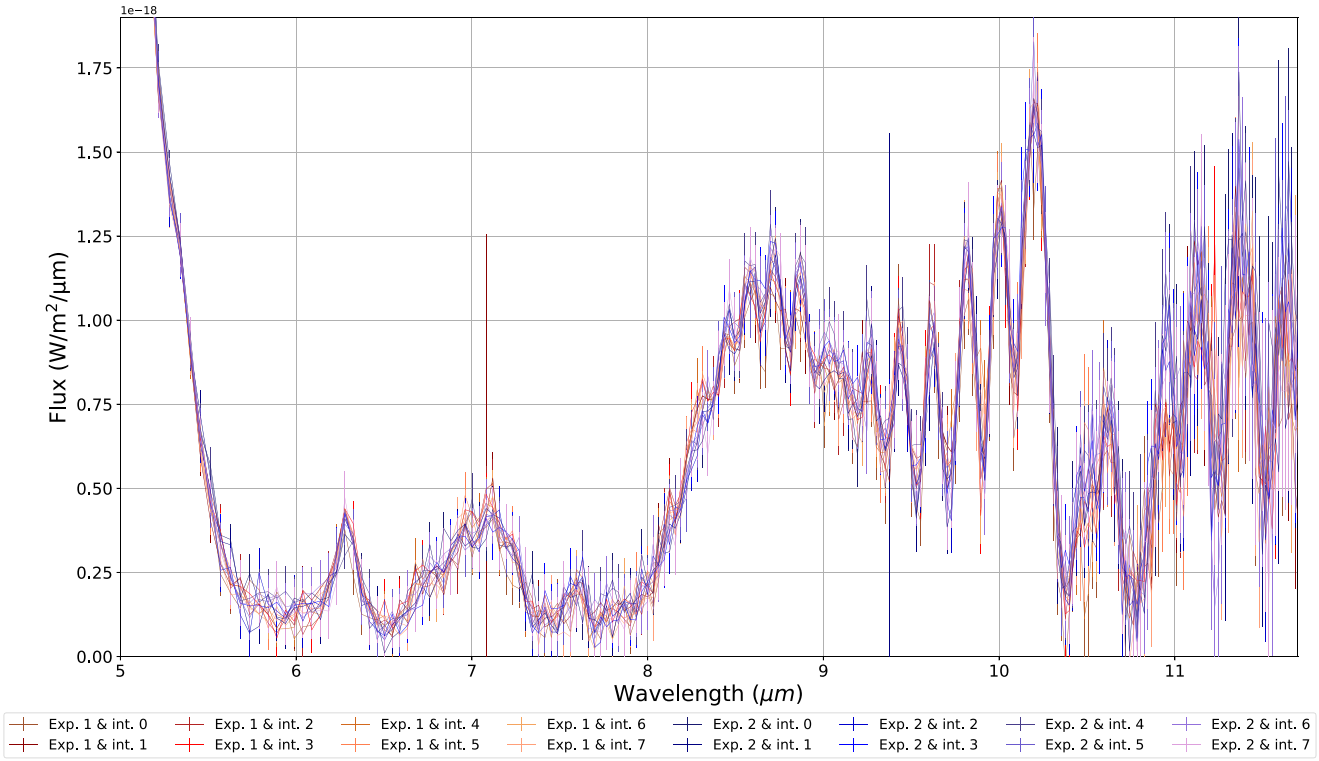

Figure 9. Spectra extracted from every integration after our "background rescaling" step. The compatibility of the integrations constrains the variability of the planet over the 4 hr period in which they were taken.

ORCID iDs

Maël Voyer https://orcid.org/0000-0002-0615-9253
Quentin Changeat https://orcid.org/0000-0001-6516-4493
Pascal Tremblin https://orcid.org/0000-0001-6172-3403
Rens Waters https://orcid.org/0000-0002-5462-9387
Manuel Güdel https://orcid.org/0000-0001-9818-0588
Thomas Henning https://orcid.org/0000-0002-1493-300X
Olivier Absil https://orcid.org/0000-0002-4006-6237
David Barrado https://orcid.org/0000-0002-5971-9242
Anthony Boccaletti https://orcid.org/0000-0001-9353-2724
Jeroen Bouwman https://orcid.org/0000-0003-4757-2500
Alain Coulais https://orcid.org/0000-0001-6492-7719
Leen Decin https://orcid.org/0000-0002-5342-8612
Adrian M. Glauser https://orcid.org/0000-0001-9250-1547
John Pye https://orcid.org/0000-0002-0932-4330
Alistair Glasse https://orcid.org/0000-0002-2041-2462
René Gastaud https://orcid.org/0009-0007-5200-1362
Sarah Kendrew https://orcid.org/0000-0002-7612-0469
Polychronis Patapis https://orcid.org/0000-0001-8718-3732
Daniel Rouan https://orcid.org/0000-0002-2352-1736
Ewine F. van Dishoeck https://orcid.org/0000-0001-7591-1907
Göran Östlin https://orcid.org/0000-0002-3005-1349
Tom P. Ray https://orcid.org/0000-0002-2110-1068
Gillian Wright https://orcid.org/0000-0001-7416-7936

References

Abel, M., Frommhold, L., Li, X., & Hunt, K. L. C. 2011, JPCA, 115, 6805
Abel, M., Frommhold, L., Li, X., & Hunt, K. L. C. 2012, JChPh, 136, 044319
Alonso, R., Rodríguez-Gil, P., Izquierdo, P., et al. 2021, A&A, 649, A131
Al-Refaie, A. F., Changeat, Q., Venot, O., Waldmann, I. P., & Tinetti, G. 2022, ApJ, 932, 123
Al-Refaie, A. F., Changeat, Q., Waldmann, I. P., & Tinetti, G. 2021, ApJ, 917, 37
Asplund, M., Grevesse, N., Sauval, A. J., & Scott, P. 2009, ARA&A, 47, 481
Barrado, D., Mollière, P., Patapis, P., et al. 2023, Natur, 624, 263
Beiler, S. A., Cushing, M. C., Kirkpatrick, J. D., et al. 2023, ApJL, 951, L48
Beiler, S. A., Cushing, M. C., Kirkpatrick, J. D., et al. 2024, ApJ, 973, 107
Bouchet, P., García-Marín, M., Lagage, P. O., et al. 2015, PASP, 127, 612
Bradley, L., Sipőcz, B., Robitaille, T., et al. 2024, astropy/photutils: v1.13.0, Zenodo, doi:10.5281/zenodo.12585239
Buchner, J., Georgakakis, A., Nandra, K., et al. 2014, A&A, 564, A125
Burrows, A., Hubeny, I., Budaj, J., & Hubbard, W. B. 2007, ApJ, 661, 502
Burrows, A., Sudarsky, D., & Lunine, J. I. 2003, ApJ, 596, 587
Bushouse, H., Eisenhamer, J., Dencheva, N., et al. 2024, JWST Calibration Pipeline, v1.14.0, Zenodo, doi:10.5281/zenodo.7038885
Changeat, Q., Bardet, D., Chubb, K., et al. 2025, A&A, submitted
Changeat, Q., Edwards, B., Waldmann, I. P., & Tinetti, G. 2019, ApJ, 886, 39
Changeat, Q., Skinner, J. W., Cho, J. Y. K., et al. 2024, ApJS, 270, 34
Chubb, K. L., Rocchetto, M., Yurchenko, S. N., et al. 2021, A&A, 646, A21
Cox, A. N. 2015, Allen's Astrophysical Quantities (Berlin: Springer)
Curtis, D., Rajaram, B., Toon, O., & Tolbert, M. 2005, ApOpt, 44, 4102
Edwards, B., Tsiaras, A., Changeat, Q., & Yip, K. H. 2024, RASTI, 3, 415
Feroz, F., Hobson, M. P., & Bridges, M. 2009, MNRAS, 398, 1601
Fletcher, L. N., Gustafsson, M., & Orton, G. S. 2018, ApJS, 235, 24
Fonte, S., Turrini, D., Pacetti, E., et al. 2023, MNRAS, 520, 4683
Gänsicke, B. T., Koester, D., Farihi, J., et al. 2012, MNRAS, 424, 333
Howett, C. J. A., Carlson, R. W., Irwin, P. G. J., & Calcutt, S. B. 2007, JOSAB, 24, 126
Kass, R. E., & Raftery, A. E. 1995, JASA, 90, 773
Kothari, H., Cushing, M. C., Burningham, B., et al. 2024, ApJ, 971, 121
Kühnle, H., Patapis, P., Mollière, P., et al. 2024, arXiv:2410.10933
Leggett, S. K., Dupuy, T. J., Morley, C. V., et al. 2019, ApJ, 882, 117
Leggett, S. K., & Tremblin, P. 2023, ApJ, 959, 86
Li, G., Gordon, I. E., Rothman, L. S., et al. 2015, ApJS, 216, 15
Lodders, K., & Fegley, B. 2002, Icar, 155, 393
Luhman, K. L., Burgasser, A. J., & Bochanski, J. J. 2011, ApJL, 730, L9
Luhman, K. L., Burgasser, A. J., Labbé, I., et al. 2012, ApJ, 744, 135
Malamud, U. 2024, arXiv:2403.07427
Marley, M. S., Saumon, D., Visscher, C., et al. 2021, ApJ, 920, 85
Miles, B. E., Biller, B. A., Patapis, P., et al. 2023, ApJL, 946, L6

Miles, B. E., Skemer, A. J. I., Morley, C. V., et al. 2020, AJ, 160, 63
Polyansky, O. L., Kyuberis, A. A., Zobov, N. F., et al. 2018, MNRAS, 480, 2597
Pyo, J., Matsumoto, T., Jeong, W.-S., & Matsuura, S. 2012, ApJ, 760, 102
Pyo, J., Ueno, M., Kwon, S. M., et al. 2010, A&A, 523, A53
Reach, W. T., Morris, P., Boulanger, F., & Okumura, K. 2003, Icar, 164, 384
Rieke, G. H., Wright, G. S., Böker, T., et al. 2015, PASP, 127, 584
Rigby, J., Perrin, M., McElwain, M., et al. 2023, PASP, 135, 048001
Rogers, L. K., Bonsor, A., Xu, S., et al. 2024, MNRAS, 532, 3866
Saumon, D., & Marley, M. S. 2008, ApJ, 689, 1327
Sousa-Silva, C., Al-Refaie, A. F., Tennyson, J., & Yurchenko, S. N. 2015, MNRAS, 446, 2337
Subasavage, J. P., Jao, W.-C., Henry, T. J., et al. 2009, AJ, 137, 4547
Sumlin, B. J., Heinson, W. R., & Chakrabarty, R. K. 2018, JQSRT, 205, 127
Tennyson, J., Yurchenko, S. N., Al-Refaie, A. F., et al. 2016, JMoSp, 327, 73
Tremblin, P., Padioleau, T., Phillips, M. W., et al. 2019, ApJ, 876, 144
Trotta, R. 2008, ConPh, 49, 71
Tu, Z., Wang, S., & Liu, J. 2024, ApJ, 976, 82
Veras, D. 2021, Oxford Research Encyclopedia of Planetary Science, Vol. 1 (Oxford: Oxford Univ. Press)
Wright, G. S., Rieke, G. H., Glasse, A., et al. 2023, PASP, 135, 048003
Xu, S., Diamond-Lowe, H., MacDonald, R. J., et al. 2021, AJ, 162, 296
Xu, S., Dufour, P., Klein, B., et al. 2019, AJ, 158, 242
Xuan, J. W., Mérand, A., Thompson, W., et al. 2024, Natur, 634, 1070
Yip, K. H., Changeat, Q., Edwards, B., et al. 2021, AJ, 161, 4
Yurchenko, S. N., Barber, R. J., & Tennyson, J. 2011, MNRAS, 413, 1828
Yurchenko, S. N., Mellor, T. M., Freedman, R. S., & Tennyson, J. 2020, MNRAS, 496, 5282
Yurchenko, S. N., & Tennyson, J. 2014, MNRAS, 440, 1649
Zalesky, J. A., Line, M. R., Schneider, A. C., & Patience, J. 2019, ApJ, 877, 24